ChemComm

COMMUNICATION

View Article Online
View Journal | View Issue

Cite this: *Chem. Commun.*, 2025, **61**, 11951

Received 9th May 2025,
Accepted 20th June 2025

DOI: 10.1039/d5cc02655e

rsc.li/chemcomm

Evaluating CO_2-to-formic acid electrocatalysts in different device configurations†

Thuy-Duong Nguyen-Phan, *[a] James E. Ellis,[ab] Bret H. Howard[a] and Douglas R. Kauffman *[a]

We evaluated CO_2 electroreduction differences of three materials in aqueous H-cell, gas diffusion electrode (GDE) half-cell, and full-cell electrolyzer devices. Mass-transport limited catalyst differences in H-cells become more apparent in gas-fed GDE half-cells; however, voltage contributions from device components can mask cathode differences in full-cell devices until high current density.

Low temperature electrochemical CO_2 reduction (CO_2R) is a promising approach to convert a low-value waste gas into industrially-relevant chemicals.[1–5] Liquid formic acid (FA) is one product of interest with use in fuel cells, agricultural, chemicals, and pharmaceutical applications.[2,3,6–13] Recent efforts have focused on improving FA production through electrocatalyst development and optimizing the operating conditions, cell components, and device configuration.[3–5,8–10,12–19] However, differences between the electrochemical device architectures used to screen and validate CO_2R electrocatalysts makes it difficult to evaluate material improvements and compare against literature results.

CO_2R reports have historically used aqueous H-cells filled with CO_2 saturated aqueous catholyte to screen and demonstrate electrocatalyst materials.[3,8–10,20] However, the low solubility (34.2 mmol L^{-1}) and diffusivity ($\sim 2 \times 10^{-9}$ m^2 s^{-1}) of CO_2 dissolved in aqueous electrolyte[20,21] limits current densities and this device configuration does not represent a deployable full-cell electrolyzer design. The field has subsequently shifted to gas diffusion electrodes (GDEs) that deliver gaseous CO_2 to the cathode for more efficient mass transfer, better catalyst utilization, and the ability to achieve industrially relevant current densities.[1,3,4,9,10,13,14,16,18,19,22]

GDE half-cells largely mimic full-cell device architectures but include a reference electrode to quantify cathode voltages and kinetics. The cathode voltages can be corrected for the *iR* drop associated with uncompensated solution resistance ($E_{cathode}$-*iR*) and referenced against the reversible hydrogen electrode (RHE). Both zero-gap (cathode directly interfaced to an ion exchange membrane) and single-gap (thin flowing catholyte layer separating cathode and membrane) full-cell electrolyzer devices have been demonstrated for CO_2 to FA.[4,9–11,18–20,22–24] The reported full-cell voltage (E_{cell}) represents the absolute anode–cathode voltage difference and includes contributions from the cathode, anode, membrane and catholyte (if used) that are difficult to deconvolute.

It is common to see catalyst screening studies conducted in H-Cell or GDE half-cell devices, but it is not often shown how apparent catalyst performance differences translate between aqueous H-cell, GDE half-cell, and full cell device architectures. In this work, we compared the CO_2R to FA performance of commercially-available SnO_2, Bi_2O_3, and In_2O_3 electrocatalysts in aqueous H-cell, GDE half-cell, and full cell device configurations to understand how device architecture impacts apparent catalyst activity (Fig. S1 and S2, ESI†). Tin, bismuth, and indium-based materials are well known electrocatalysts to convert CO_2 into formic acid or formate and they have been commonly investigated in various cell configurations.[9–12,16,24–26]

Detailed methods are described in the ESI,† but briefly, aqueous H-cells contained a 0.075 cm^2 cathode and Ag/AgCl reference electrode submerged in 60 mL of CO_2-saturated 0.4 M K_2SO_4 catholyte, a Nafion 117 membrane, and a Pt mesh anode in 0.4 M K_2SO_4 anolyte. GDE half-cell and full-cell experiments were conducted using commercially-available hardware (Dioxide Materials), a 6.25 cm^2 cathode supplied with gaseous CO_2, a flowing 0.4 M K_2SO_4 catholyte chamber (half-cell $\sim$1.9 mL volume, full cell $\sim$1.0 mL volume), a Nafion N324 membrane, an IrO_2 anode and flowing deionized H_2O anolyte. The bulk catholyte pH in H-cell experiments was around 5.5 and the FA product was detected in the ionic formate form, while the GDE half-cell and full-cell experiments produced a more acidified FA product stream (pH 2.5–4.5). However, we simply refer to the product as FA in all cases. A miniature reversible hydrogen

[a] *National Energy Technology Laboratory, 626 Cochran Mill Road, Pittsburgh, PA 15236, USA. E-mail: ThuyDuong.NguyenPhan@netl.doe.gov, Douglas.Kauffman@netl.doe.gov*

[b] *NETL Support Contractor, 626 Cochran Mill Road, Pittsburgh, PA 15236, USA*

† Electronic supplementary information (ESI) available. See DOI: https://doi.org/10.1039/d5cc02655e

reference electrode was inserted into the flowing catholyte chamber to quantify GDE half-cell cathode potentials. All H-Cell and GDE half-cell and cathode potentials were 100% *iR*-corrected for the uncompensated resistance and referenced against the RHE scale.[27] Full-cell E_{cell} values were not corrected.

Typical figures of merit for H-cell and GDE half-cell experiments include the product faradaic efficiency (FE) and partial current density *versus* $E_{cathode}$-*iR* (V *vs.* RHE), where FE and partial current density represent the fraction of the total electrons and current density used to form the product (eqn (S1) and (S2), ESI†). Fig. 1 summarizes the FA partial current density and formic acid FE (FE_{FA}) *versus* the cathode potential for Bi_2O_3, SnO_2 and In_2O_3 in the aqueous H-cell and GDE half-cell devices. All three catalysts demonstrated similar apparent CO_2R onset potentials, Tafel slopes, and partial current densities in the H-Cell (Fig. 1A, B and Fig. S3A, ESI†). They all demonstrated initially low FE_{FA} values at smaller cathode overpotentials that increased towards larger overpotentials, but SnO_2 showed consistently lower FE_{FA} than Bi_2O_3 and In_2O_3 due to higher H_2 and CO formation (Fig. S4, ESI†). Bi_2O_3 produced slightly higher partial current density than In_2O_3 and SnO_2 at some potentials, but the similar current density profiles suggest mass transport limitations associated with converting dissolved CO_2 may hinder the apparent catalyst activity towards larger cathode potentials.

Fig. 1C, D and Fig. S5, S6 (ESI†) compare catalyst performance in the GDE half-cell device over a comparable $E_{cathode}$-*iR* range used for H-cell experiments. The catalysts demonstrated a similar FE_{FA} trend that increased with cathode potential (Fig. 1C). Bi_2O_3 and In_2O_3 both demonstrated >90% FE_{FA} between −1.1 V and −1.4 V *vs.* RHE, but SnO_2 plateaued around 80% FE_{FA}. Notably, the catalysts produced larger current density in the gas-fed GDE half-cell configuration than in the H-Cell (Fig. 1D). Bi_2O_3 partial current density now obviously exceeded SnO_2 and In_2O_3 at higher overpotentials, albeit with a larger apparent CO_2R onset potential than the other catalysts. GDE half-cell results also revealed that the linear Tafel region extended to larger partial current densities than in the H-cell device (Fig. S3, ESI†). This observation points towards reduced mass transfer limitations in the gas-fed GDE half-cell, and differences in CO_2R activity between the three catalysts are now well observed. Taken together, the results in Fig. 1 suggest H-cell devices may mask intrinsic catalyst activity differences and identify gas-fed GDE half-cell device as a better choice for comparing catalysts' cathodic CO_2R performance.

We have shown that GDE half-cells can differentiate cathodic catalyst performance more clearly than H-cells, but the literature does not often discuss how cathodic CO_2R catalyst activity differences translate to full-cell devices. Fig. 2 and Fig. S5–S7 (ESI†) confirm that the three catalysts individually showed similar partial current densities and FE_{FA} in the GDE half- and full-cell configurations. In this convention, the partial current density (left axis) and FE_{FA} (right axis) are plotted as a function of total applied current density, and deviations between the applied and partial current densities represent reduced FE_{FA}. Bi_2O_3 maintained high FE_{FA} around 90% between 50–500 mA cm^{-2} applied current density and produced a maximum FA partial current density between 400–460 mA cm^{-2} in both GDE half-cell and full-cell devices. In_2O_3 and SnO_2 demonstrated reduced (60–80%) FE_{FA} at applied current densities >400 mA cm^{-2} that limited their maximum FA partial current density to 250–400 mA cm^{-2} in both GDE half-cell and full cell devices.

Catalysts did show lower maximum partial current density in the GDE-half cell device than in the full-cell device. We hypothesize this may stem from mass transport differences associated with thicker catholyte flow chamber used to house the reference electrode in the GDE half-cell device (3 mm thick chamber, 1.9 mL flowing catholyte volume) compared with the thinner catholyte chamber used in full-cell device experiments (1.6 mm thick chamber, 1 mL flowing catholyte volume). However, these results do show that both GDE half-cell and full cell devices can produce similar FE_{FA} up to very large current densities.

Full-cell E_{cell} values include resistance contributions from the anode, ion exchange membrane, cell hardware and solution

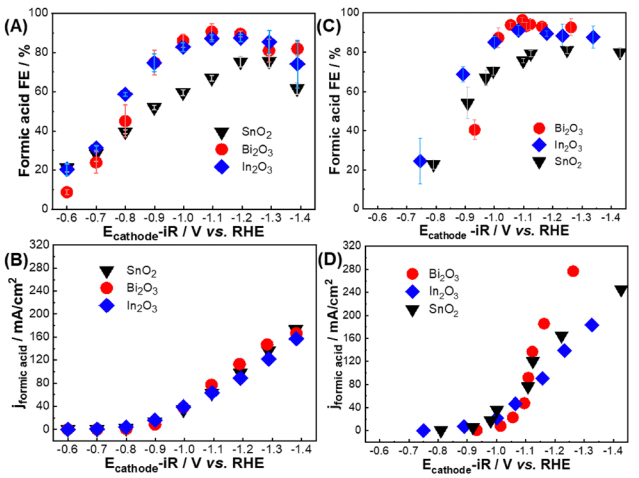

Fig. 1 Formic acid FE and partial current densities as function of *iR*-corrected cathode potential ($E_{cathode}$-*iR*) for Bi_2O_3, In_2O_3, and SnO_2 in (A, B) aqueous H-cell and (C, D) GDE half-cell configurations. Note that same *Y*-axis and *X*-axis scales were plotted for (B) and (D) panels to clearly demonstrate the difference between aqueous H-cell and GDE half-cell current densities over a similar potential range. GDE half-cell results over a larger potential range are shown in Fig. S4 (ESI†).

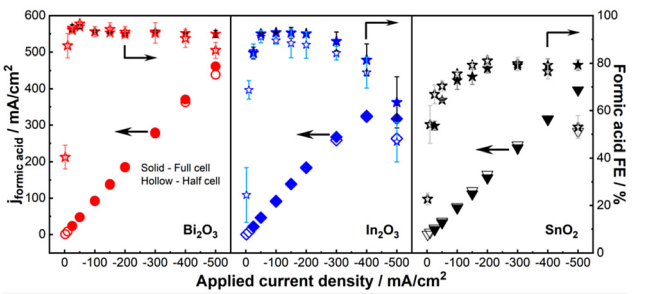

Fig. 2 Comparison of FA partial current densities and FE_{FA} for all three catalysts as a function of applied current density in half-cell (hollow) and full cell (solid).

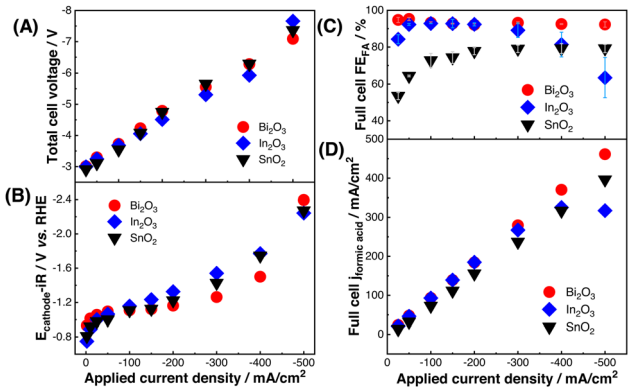

Fig. 3 (A) Total full-cell cell voltages (E_{cell}) and (B) GDE half-cell *iR*-corrected cathode potentials ($E_{cathode}$-*iR*) *versus* total applied current density. Comparison of (C) FE_{FA} and (D) FA partial current density *versus* total applied current density in the full-cell device for Bi_2O_3, In_2O_3, and SnO_2.

resistance, and Fig. 3A demonstrates that all three cathode catalysts operated with similar E_{cell} values in the full-cell device. We acknowledge these cell voltages are larger than typically shown for zero-gap devices, but these values and energy efficiencies (Fig. S7D, ESI†) are comparable to previous reports using similar flowing catholyte device configurations.[3,8,10,13,20,28] The field is actively developing other device configurations (*i.e.* zero gap and MEA) and alternative anode reactions to reduce E_{cell} and improve energy efficiency.[3,8–10,18,20,22,29,30]

Fig. 3B also reports the GDE half-cell E-$iR_{cathode}$ values over the same applied current density range. While this comparison is not a quantitative voltage break down of the full-cell components,[13] these results highlight that *iR*-corrected cathode voltage is small compared to the total full-cell E_{cell}. Moreover, the 100–300 mV E-$iR_{cathode}$ difference observed between catalysts in GDE half-cell experiments did not translate to meaningful changes in the full-cell E_{cell} values. This suggests that half-cell partial current density and E-$iR_{cathode}$ differences may not significantly impact single-gap, flowing catholyte full-cell performance unless those differences are very large.

The observation that catalyst $E_{cathode}$-*iR* differences do not significantly impact full-cell E_{cell} identifies FE_{FA} as a key performance metric. Fig. 3C and D compare the full-cell performance of the three catalysts. Bi_2O_3 sustained >90% FE_{FA} between 50–500 mA cm^{-2} applied current and it produced a maximum FA partial current density of ~460 mA cm^{-2}. In_2O_3 also sustained ~90% FE_{FA} up to 300 mA cm^{-2} applied current density, but decreasing FE_{FA} above this point (60–80% FE_{FA}) limited the In_2O_3 maximum partial current density to ~320 mA cm^{-2}. SnO_2 FE_{FA} never exceeded 80% in the full-cell device and its partial current density was consistently lower than Bi_2O_3. Both SnO_2 and In_2O_3 also experienced particle agglomeration during electrolysis that may have further contributed to them producing lower maximum partial current density than Bi_2O_3, which transformed into two-dimensional sheet-like structures during CO_2R (Fig. S8, ESI†).[8,26] Fig. 3 results confirm that FE_{FA} differences observed in GDE half-cell experiments translate to full-cell operation, whereas the catalysts' potential-dependent partial current density and cathodic $E_{cathode}$-*iR* did not substantially impact full cell performance. We hypothesize the comparatively small contribution of $E_{cathode}$-*iR* to the total E_{cell} made FE_{FA} deviations the main differentiator between catalyst performance in the full-cell device. In addition, good correlation between half-cell and full-cell partial current densities indicates that the half-cell performance can inform full-cell performance at moderate current densities (Fig. S9, ESI†).

Finally, Fig. 4 and Fig. S10 (ESI†) confirm the catalysts maintained good stability and selectivity over 24 hours of operation at 100 mA cm^{-2} applied current density in the full-cell device, with FE_{FA} of 93 ± 2% for Bi_2O_3, 92 ± 1% for In_2O_3, and 78 ± 5% for SnO_2 and total cell voltages between 3.8 and 4.3 V.

In summary, we evaluated three commercially-available CO_2 to FA electrocatalysts in three commonly-used cell configurations, including H-cell, GDE half-cell and full-cell devices. Limitations associated with converting dissolved CO_2 in H-cells limits catalyst performance and may mask inherent activity differences. Our results show that H-cell devices may be more appropriate for specialized studies, such as comparing soluble homogeneous catalysts, rotating disk electrode experiments, single-crystals, or catalysts grown on nonporous substrates.[4,20,31,32] GDE half-cells appear to be a better tool for conducting cathode-specific kinetic studies. Their ability to produce current densities and product FEs that are comparable to full-cell devices make them a suitable screening tool to predict high-current density product selectivity in full-cells. One benefit of the single-gap, flowing catholyte GDE half-cell design is the relatively straight-forward method of isolating cathode voltages by incorporating a reference electrode into the central catholyte chamber, compared with more sophisticated membrane-based reference electrodes or anodic H_2 oxidation approaches demonstrated in some full-cell architectures.[18,22,29,30,33] However, this flowing catholyte architecture does increase full-cell E_{cell} values compared with zero-gap architectures.

Our results show that FE differences observed in half-cells do translate to full-cell performance, but that they may not become substantial in full-cell devices until higher current

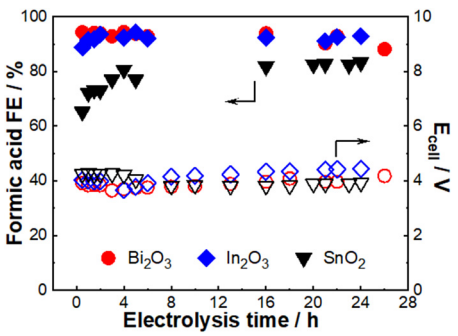

Fig. 4 Stability over 24 hours at 100 mA cm^{-2} in the full cell device.

density regimes due to the other component's resistance contributions. We suggest that catalyst development studies should include both GDE half-cell and full-cell studies to fully characterize cathode kinetics and demonstrate the translatability of apparent material improvements in relevant device architectures. We hope this study will help researchers choose the most appropriate device hardware and methodology for screening formic acid producing CO_2R catalysts in single-gap, flow catholyte electrolyzers.

This work was performed in support of the U.S. Department of Energy's Fossil Energy and Carbon Management's Carbon Conversion Program and executed through the National Energy Technology Laboratory (NETL) Research & Innovation Center's Carbon Utilization MYRP. This project was funded by the United States Department of Energy, National Energy Technology Laboratory, in part, through a site support contract. Neither the United States Government nor any agency thereof, nor any of their employees, nor the support contractor, nor any of their employees, makes any warranty, express or implied, or assumes any legal liability or responsibility for the accuracy, completeness, or usefulness of any information, apparatus, product, or process disclosed, or represents that its use would not infringe privately owned rights. Reference herein to any specific commercial product, process, or service by trade name, trademark, manufacturer, or otherwise does not necessarily constitute or imply its endorsement, recommendation, or favoring by the United States Government or any agency thereof. The views and opinions of authors expressed herein do not necessarily state or reflect those of the United States Government or any agency thereof.

Conflicts of interest

There are no conflicts to declare.

Data availability

The data supporting this article have been included as part of the ESI,† including additional methods and results in Fig. S1–S10.

Notes and references

1 C. P. O'Brien, R. K. Miao, A. Shayesteh Zeraati, G. Lee, E. H. Sargent and D. Sinton, *Chem. Rev.*, 2024, **124**, 3648–3693.
2 S. Zhai, S. Jiang, C. Liu, Z. Li, T. Yu, L. Sun, G. Ren and W. Deng, *J. Phys. Chem. Lett.*, 2022, **13**, 8586–8600.
3 A. Badgett, M. Ruth, A. Crow, G. Grim, Y. Chen, L. Hu, L. Tao, W. Smith, K. C. Neyerlin and R. Cortright, *J. Cleaner Prod.*, 2022, **351**, 131564.
4 S. Liang, N. Altaf, L. Huang, Y. Gao and Q. Wang, *J. CO_2 Util.*, 2020, **35**, 90–105.
5 J. Herranz, A. Pătru, E. Fabbri and T. J. Schmidt, *Curr. Opin. Electrochem.*, 2020, **23**, 89–95.
6 J. Eppinger and K.-W. Huang, *ACS Energy Lett.*, 2017, **2**, 188–195.
7 B. S. Crandall, T. Brix, R. S. Weber and F. Jiao, *Energy Fuels*, 2022, **37**, 1441–1450.
8 J. Zou, G. Liang, C.-Y. Lee and G. G. Wallace, *Mater. Today Energy*, 2023, **38**, 101433.
9 K. Fernández-Caso, G. Díaz-Sainz, M. Alvarez-Guerra and A. Irabien, *ACS Energy Lett.*, 2023, **8**, 1992–2024.
10 Z. M. Ghazi, D. Ewis, H. Qiblawey and M. H. El-Naas, *Carbon Capture Sci. Technol.*, 2024, **13**, 100308.
11 M. Oßkopp, A. Löwe, C. M. S. Lobo, S. Baranyai, T. Khoza, M. Auinger and E. Klemm, *J. CO_2 Util.*, 2022, **56**, 101823.
12 C. Xia, P. Zhu, Q. Jiang, Y. Pan, W. Liang, E. Stavitski, H. N. Alshareef and H. Wang, *Nat. Energy*, 2019, **4**, 776–785.
13 Y. Chen, A. Vise, W. E. Klein, F. C. Cetinbas, D. J. Myers, W. A. Smith, T. G. Deutsch and K. C. Neyerlin, *ACS Energy Lett.*, 2020, **5**, 1825–1833.
14 H. Yang, J. J. Kaczur, S. D. Sajjad and R. I. Masel, *J. CO_2 Util.*, 2020, **42**, 101349.
15 L. Fan, C. Xia, P. Zhu, Y. Lu and H. Wang, *Nat. Commun.*, 2020, **11**, 3633.
16 S. Sen, S. M. Brown, M. Leonard and F. R. Brushett, *J. Appl. Electrochem.*, 2019, **49**, 917–928.
17 B.-U. Choi, Y. C. Tan, H. Song, K. B. Lee and J. Oh, *ACS Sustainable Chem. Eng.*, 2021, **9**, 2348–2357.
18 L. Hu, J. A. Wrubel, C. M. Baez-Cotto, F. Intia, J. H. Park, A. J. Kropf, N. Kariuki, Z. Huang, A. Farghaly, L. Amichi, P. Saha, L. Tao, D. A. Cullen, D. J. Myers, M. S. Ferrandon and K. C. Neyerlin, *Nat. Commun.*, 2023, **14**, 7605.
19 G. Díaz-Sainz, M. Alvarez-Guerra, J. Solla-Gullón, L. García-Cruz, V. Montiel and A. Irabien, *J. CO_2 Util.*, 2019, **34**, 12–19.
20 A. Gawel, T. Jaster, D. Siegmund, J. Holzmann, H. Lohmann, E. Klemm and U.-P. Apfel, *iScience*, 2022, **25**, 104011.
21 N. Gupta, M. Gattrell and B. MacDougall, *J. Appl. Electrochem.*, 2006, **36**, 161–172.
22 H.-P. Iglesias van Montfort, S. Subramanian, E. Irtem, M. Sassenburg, M. Li, J. Kok, J. Middelkoop and T. Burdyny, *ACS Energy Lett.*, 2023, **8**, 4156–4161.
23 H. Yang, J. J. Kaczur, S. D. Sajjad and R. I. Masel, *J. CO_2 Util.*, 2017, **20**, 208–217.
24 R. I. Masel, Z. Liu, H. Yang, J. J. Kaczur, D. Carrillo, S. Ren, D. Salvatore and C. P. Berlinguette, *Nat. Nanotechnol.*, 2021, **16**, 118–128.
25 S. Sun, H. Cheng, X. Li, X. Wu, D. Zhen, Y. Wang, R. Jin and G. He, *Ind. Eng. Chem. Res.*, 2021, **60**, 1164–1174.
26 N. Han, P. Ding, L. He, Y. Li and Y. Li, *Adv. Energy Mater.*, 2020, **10**, 1902338.
27 S. Anantharaj and S. Noda, *J. Mater. Chem. A*, 2022, **10**, 9348–9354.
28 T.-D. Nguyen-Phan, L. Hu, B. H. Howard, W. Xu, E. Stavitski, D. Leshchev, A. Rothenberger, K. C. Neyerlin and D. R. Kauffman, *Sci. Rep.*, 2022, **12**, 8420.
29 K. Fernández-Caso, A. Peña-Rodríguez, J. Solla-Gullón, V. Montiel, G. Díaz-Sainz, M. Alvarez-Guerra and A. Irabien, *J. CO_2 Util.*, 2023, **70**, 102431.
30 Y. Zhang, J. Lan, F. Xie, M. Peng, J. Liu, T.-S. Chan and Y. Tan, *ACS Appl. Mater. Interfaces*, 2022, **14**, 25257–25266.
31 X. Deng, D. Alfonso, T.-D. Nguyen-Phan and D. R. Kauffman, *ACS Catal.*, 2022, **12**, 5921–5929.
32 C. Costentin, M. Robert, J.-M. Savéant and A. Tatin, *Proc. Natl. Acad. Sci. U. S. A.*, 2015, **112**, 6882–6886.
33 K. U. Hansen, L. H. Cherniack and F. Jiao, *ACS Energy Lett.*, 2022, **7**, 4504–4511.

